JOURNAL OF GUIDANCE, CONTROL, AND DYNAMICS
Vol. 25, No. 6, November–December 2002

Dynamics/Control of a Radio Telescope Receiver Supported by a Tethered Aerostat

Meyer Nahon*
McGill University, Montreal, Quebec H3A 2K6, Canada
and
Gabriele Gilardi† and Casey Lambert‡
University of Victoria, Victoria, British Columbia V8W 3P6, Canada

Canadian researchers have proposed a design for a new radio telescope consisting of an array of very large reflectors. A large multitethered aerostat will be used to support each reflector's receiver. The length of each tether can be adjusted by ground-based winches, and active control is used to overcome the effects of wind turbulence on the aerostat. To aid in the system's mechanical and controller design, a computer model has been developed, including models of the tethers and the aerostat. Two types of aerostat have been considered: spherical and streamlined. A wind turbulence model is incorporated to provide disturbance to the system. Controllers are used to adjust the tether lengths based on feedback of the receiver's position. The model is used to optimize the control gains. We find that, with 50 kW available at each winch, it is possible to maintain the receiver's position within 85 cm of its desired location, even in the worst-case configuration.

Nomenclature

A	=	cross-sectional area of cable element, or fin aspect ratio
A_f	=	fin planform area
a	=	constant in von Kármán turbulence model
C_D, C_{D0}	=	fin drag coefficient, fin parasitic drag coefficient
C_d	=	normal drag coefficient of cable element, spherical aerostat, or receiver
C_L	=	fin lift coefficient
C_v	=	cable damping coefficient
$(Cd_h)_0$, $(Cd_c)_h$	=	hull zero-angle axial and crossflow drag coefficients
D_h	=	drag force acting on hull
D_s	=	aerodynamic drag force on receiver or spherical aerostat
$\boldsymbol{D}^i$	=	aerodynamic drag force on cable element, $[D^i_{p1}, D^i_{p2}, D^i_q]^T$
d_c	=	diameter of cable element
d_s	=	aerostat or receiver diameter
E	=	effective Young's modulus of cable element
$E_{\max}$	=	maximum error in receiver position
e	=	fin efficiency factor
e_j	=	error in distance between winch and receiver
f_p, f_q	=	aerodynamic loading functions
g	=	gravitational acceleration
h, h_g	=	height and gradient height in the planetary boundary layer
I_1, I_3	=	hull-related geometric quantities
J_1, J_3	=	hull-related geometric quantities
k_P, k_D, k_I	=	proportional, derivative, and integral controller gains
k_1, k_3	=	axial and lateral added-mass coefficients
L, L_0, ΔL	=	tether length, initial length, and change in length
L_u, L_v, L_w	=	turbulence scale lengths in longitudinal, lateral, and vertical directions
l^i, l^i_u	=	stretched and unstretched length cable element
M_{nose}	=	moment about the nose acting on hull
m_c	=	mass of cable element
N	=	number of discrete spectral bands considered in turbulence spectrum
N_h	=	transverse force acting on hull
n_t, n_l	=	number of elements in each tether and in the leash
$P_{\max}$	=	maximum winch power required
P^i_q	=	tension due to internal damping in cable element
p_1, p_2, q	=	axes of the element-fixed reference frame
$\boldsymbol{p}$, $\boldsymbol{p}_d$	=	actual and desired position of receiver
$\boldsymbol{p}_{Wj}$	=	winch position
q_0	=	steady-state dynamic pressure, $\rho V_B^2/2$
R	=	focal distance
$\boldsymbol{r}^i$	=	position of cable node i, $[r^i_X \;\; r^i_Y \;\; r^i_Z]^T$
S_h	=	hull reference area, (hull volume)$^{2/3}$
T_i	=	tether tension at winch i
T^i_q	=	tension due to structural stiffness in cable element
t, T	=	number of tethers or time, and total time to complete a slewing maneuver
U, U_g	=	wind speed at height h and at gradient height h_g
$\boldsymbol{U}^i$	=	local air velocity at node i due to mean wind and turbulence, $[U^i_X, U^i_Y, U^i_Z]^T$
$\boldsymbol{V}$	=	local air velocity at component reference point, $[u, v, w]^T$
V_B	=	total velocity of hull reference point
v_g	=	gust velocity
$\boldsymbol{v}^i$	=	velocity of geometric center of cable element with respect to surrounding air, $[v^i_{p1}, v^i_{p2}, v^i_q]^T$
$\boldsymbol{v}_s$	=	local velocity of the geometric center of the aerostat or receiver
W^i	=	weight of cable element
X, Y, Z	=	axes of the inertial reference frame
α	=	angle of attack
β	=	sideslip angle

Received 2 November 2001; revision received 1 July 2002; accepted for publication 24 July 2002.

*Associate Professor, Department of Mechanical Engineering, 817 Sherbrooke Street West. Senior Member AIAA.
†Research Associate, Department of Mechanical Engineering, P.O. Box 3055.
‡Graduate Student, Department of Mechanical Engineering, P.O. Box 3055. Student Member AIAA.

γ	=	wind power law exponent
ε	=	strain of cable element
η	=	relative angle between cable element and incident fluid flow
η_k	=	hull efficiency factor
θ_w	=	wind direction
θ_{za}, θ_{az}	=	zenith and azimuth angles of telescope pointing
ρ	=	local air density
ρ_c	=	density of cable element
$\sigma_u, \sigma_v, \sigma_w$	=	turbulence intensities in longitudinal, lateral, and vertical directions
Φ_u, Φ_v, Φ_w	=	turbulence spectra in longitudinal, lateral, and vertical directions
φ_i	=	phase angle for ith turbulence spectral component
ψ, θ, ϕ	=	yaw, pitch, and roll angles
Ω	=	wave number in turbulence model

I. Introduction

RADIO astronomers from around the world have focused recently on the need for a new radio telescope that would enable the direct observation of the formation and evolution of galaxies from gases in the universe.[1] To do this requires an increase in sensitivity of roughly two orders of magnitude over existing radio telescope arrays, to a collecting area of 10^6 m^2, and this resulted in a concept dubbed the Square Kilometer Array. One such conceptual design originates from the National Research Council of Canada's Herzberg Institute of Astrophysics and consists of an array of about 30 very large antennas. The proposed novel antenna design,[2,3] one of which is depicted in Fig. 1, is called the Large Adaptive Reflector (LAR). The LAR design is based on the premise that building a large-scale steerable radio antenna will require new concepts in the design of structures to achieve the required strength and stiffness at a reasonable cost. Preliminary estimates indicate that this telescope concept offers an order of magnitude improvement in cost per square meter of collecting area over traditional designs of large parabolic antennas.[3]

The LAR design includes two central components. The first is a 200-m-diam parabolic reflector, with a focal length of 500 m, composed of actuated panels, mounted on the ground. The second component is a focal package held aloft at a height of 500 m by a large helium balloon (aerostat) and a system of three or more taut tethers. This tension structure is large enough that it filters out all but the lowest frequency turbulence and is stiff enough that it effectively resists wind forces. The telescope is steered by modifying the shape of the reflector and simultaneously changing the lengths of the tethers with winches so that the receiver is positioned on the surface of a hemisphere of radius $R = 500$ m, centered at the center of the reflector. It is also envisioned that the variable-length tethers will allow some measure of control of the receiver position in response to disturbances such as wind gusts.

Tethered and moored aerostat systems have received limited attention in the literature,[4,5] and these have usually consisted of large streamlined aerostats constrained by a single tether. These studies have focused on the open-loop (uncontrolled) behavior of such systems. One key issue in modeling these systems is that of determination of the aerodynamic characteristics of the aerostat.[6,7] Some earlier work at the National Research Council of Canada[8] dealt with a triple-tethered aerostat system, but focused primarily on its static or steady-state performance. Interestingly, U.S. Air Force researchers

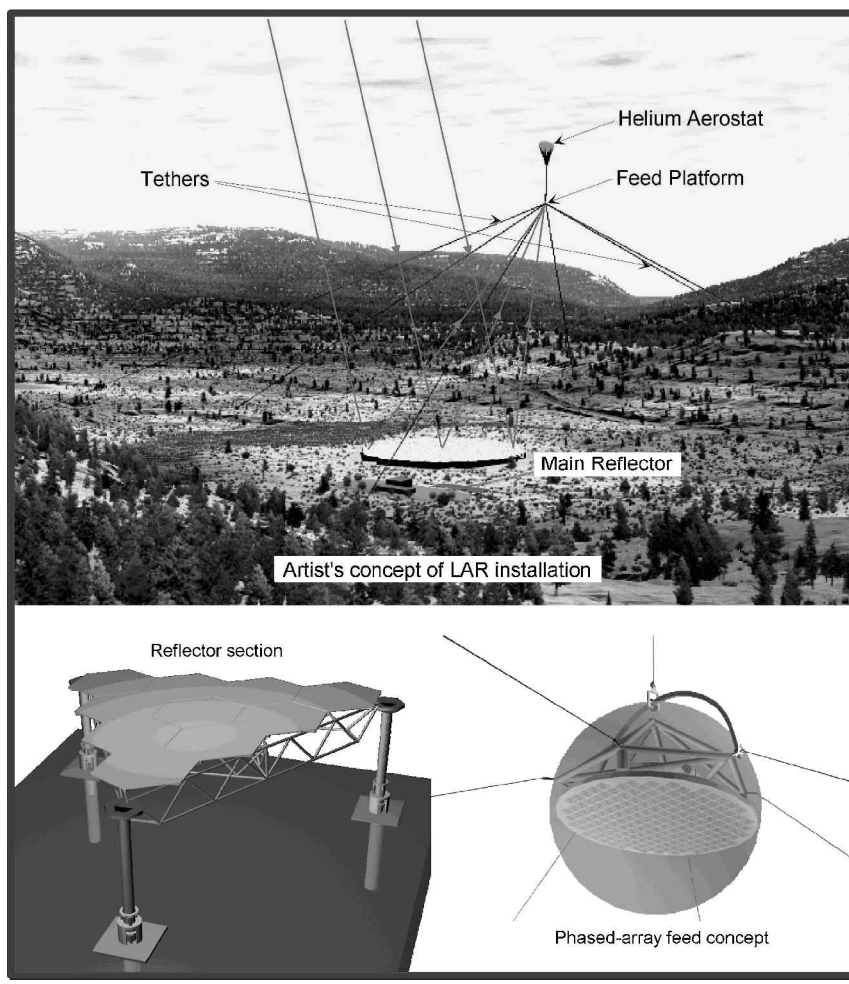

Fig. 1 LAR installation; details of one of the 150 main reflector sections and the prime-focus phased-array feed concept are shown at the bottom.[8]

performed an experimental evaluation of a similar system[9,10] and found that the tritether arrangement was much more stable than an equivalent single-tethered system.

A one-third scale prototype is presently being constructed as a proof of concept for this system. However, a mathematical model and a computer simulation can also be used to good advantage. The simulation can be used to weigh alternative design options, determine how typical gusts are likely to affect the receiver positioning accuracy, and perform preliminary evaluation of the controller architecture.

This paper discusses the modeling and control of the tethered aerostat subsystem. A model of the planetary boundary-layer mean wind and turbulence is implemented to investigate the effect of these disturbances on the system. The effectiveness of the tether winches at controlling the receiver position is evaluated using a simple controller consisting of independent proportional–integral–derivative (PID) loops on each tether. The model is used to optimize the control gains. Results are shown to highlight the effect of aerostat type (spherical or streamlined) on the system performance.

II. System Model

As shown in Fig. 1, the complete tethered aerostat subsystem consists of the following elements: 1) an aerostat of 40-kN gross lift; 2) a leash (short cable) joining the aerostat to the receiver below it; 3) the receiver, which is enclosed in a spherical shell; 4) a series of three to six elastic tethers from the ground to the confluence point at the receiver; and 5) a winch at the base of each tether. It is assumed that a global positioning system is mounted at the receiver to provide real-time measurement of the receiver position to be used in a feedback loop for actuating the winches. The modeling of each component is now discussed.

A. Cable Model

This work uses a lumped-mass model of the cables to model their dynamic behavior. In this type of model, the continuous cable is first discretized into elements. The mass of each element is lumped at its endpoints (called nodes). The internal stiffness and damping characteristics of the cable are modeled as lumped parameter stiffness and damping elements connecting those nodes. This effectively neglects the effects of bending stiffness because the dominant forces are due to tension. This type of model, illustrated in Fig. 2, has been validated for a variety of underwater systems with excellent agreement with in-field measurements.[11,12]

Two distinct types of orthogonal reference frame are used in the development of the mathematical model, an inertial reference frame and a series of body-fixed reference frames placed at the nodes along the cables. The inertial reference frame (X, Y, Z) is defined with its origin located at the ground, at the center of the three tether attachment points. The X axis is in the horizontal plane and directed from the origin of the inertial frame to the base attachment point of tether 1. The Z axis is vertical and positive upward. Finally, the Y axis completes a right-handed coordinate system. The elemental body-fixed frame (p_1, p_2, q) is defined relative to each cable element, where p_1 and p_2 are the local normal and binormal directions and q is the local tangent to the cable. Figure 3 shows the inertial reference frame, with its origin translated to coincide with node i-1,

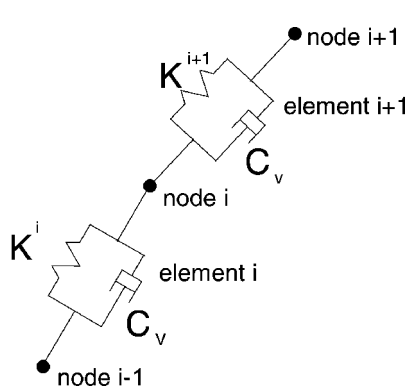

Fig. 2 Cable element and node representation.

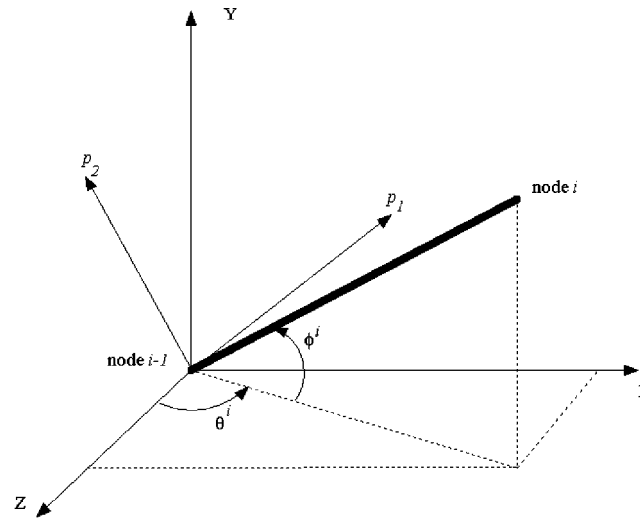

Fig. 3 The *i*th cable element.

as well as the p_1 and p_2 directions. The tangent direction is directed from node i-1 to node i.

1. Kinematics

The position of each node is described with respect to an inertial reference frame, by a three-component vector $\boldsymbol{r}^i = [r_X^i \;\; r_Y^i \;\; r_Z^i]^T$. Each cable element is considered to be a straight elastic element, subject to forces at its endpoints. This method of modeling allows each cable element to possess distinct properties, such as density and stiffness.

The orientation of each cable element is represented using a Z–Y–X (ψ, θ, ϕ) Euler angle set. These three successive rotations align the inertial frame with the ith body frame. Because the torsion of the cable is not included in the model, the ψ rotation about the inertial Z axis is constrained to zero. As shown in Fig. 2, the two remaining Euler angles can be calculated from the coordinates of the appropriate nodal endpoints as follows:

$$\theta^i = \text{atan2}\left(r_X^i - r_X^{i-1}, r_Z^i - r_Z^{i-1}\right) \tag{1}$$

The solution for ϕ^i can then be found in either of two ways, depending on which is more numerically stable:

$$\phi^i = \text{atan2}\left[-\left(r_Y^i - r_Y^{i-1}\right), \frac{\left(r_Z^i - r_Z^{i-1}\right)}{\cos\theta^i}\right] \quad \text{if} \quad \cos\theta^i \geq \sin\theta^i$$

$$\phi^i = \text{atan2}\left[-\left(r_Y^i - r_Y^{i-1}\right), \frac{\left(r_X^i - r_X^{i-1}\right)}{\sin\theta^i}\right] \quad \text{if} \quad \cos\theta^i < \sin\theta^i \tag{2}$$

2. Internal Forces

The forces in the cable model are broken down into two types: internal and external forces. Internal forces are due to axial stiffness and internal damping. These are represented schematically in Fig. 2. Forces exerted on the rope by the environment are external forces and consist of the aerodynamic drag and gravitational forces. The tension in the cable due to its axial stiffness is considered to act only in the tangential direction and is modeled by a linear function relating tension and strain:

$$T_q^i = AE\varepsilon, \qquad \varepsilon = \left(l^i - l_u^i\right)/l_u^i \tag{3}$$

where $l^i = \sqrt{[(r_X^i - r_X^{i-1})^2 + (r_Y^i - r_Y^{i-1})^2 + (r_Z^i - r_Z^{i-1})^2]}$ is the length of the ith element, l_u^i is the unstretched length of that same element, A is its cross-sectional area, and ε is the strain. The tension is set to zero if the strain becomes negative. However, this condition was never reached in the cases investigated because the aerostat buoyancy is very large in relation to the weight of the system aloft.

The friction between the braids of the cable tends to create a damping effect. Experiments on steel and synthetic cables[13] indicate that this internal damping effect can be modeled by a linear viscous term. We, therefore, assume the following relationship between damping force and strain rate:

$$P_q^i = C_v \dot{\varepsilon} l_u^i \tag{4}$$

Note, however, that this damping term is relatively small (damping ratio ~0.017) and typically has a negligible impact on the results of our simulations.

3. External Forces

The external forces acting on the cable element are those due to aerodynamic drag and gravity. The drag forces acting on the cable element can be calculated according to

$$D_{p1}^i = -\left(\tfrac{1}{2}\rho C_d d_c l_u^i\right) f_p \|\boldsymbol{v}^i\|^2 \left[v_{p1}^i \Big/ \sqrt{\left(v_{p1}^i\right)^2 + \left(v_{p2}^i\right)^2} \right]$$

$$D_{p2}^i = -\left(\tfrac{1}{2}\rho C_d d_c l_u^i\right) f_p \|\boldsymbol{v}^i\|^2 \left[v_{p2}^i \Big/ \sqrt{\left(v_{p1}^i\right)^2 + \left(v_{p2}^i\right)^2} \right]$$

$$D_q^i = -\left(\tfrac{1}{2}\rho C_d d_c l_u^i\right) f_q \|\boldsymbol{v}^i\|^2 \tag{5}$$

where $\boldsymbol{D}^i$ is the aerodynamic drag force represented in the body-fixed frame with components D_{p1}^i, D_{p2}^i, and D_q^i and $\boldsymbol{v}^i$ is the local velocity of the geometric center of the ith cable element with respect to the surrounding air, with components v_{p1}^i, v_{p2}^i, and v_q^i. These velocities must account not only for the motion of the cable element, but also the motion of the surrounding air (discussed later).

In each of the preceding equations, the drag coefficient is modified by an appropriate loading function, f_p or f_q, which are functions of η, the relative angle between the ith element and the incident fluid flow. These loading functions account for the nonlinear breakup of drag between the normal and tangential directions. Hoerner[14] provides simple expressions for these functions. Driscoll et al.[11] surveyed a number of other works to arrive at more complicated functions. These differ from Hoerner's functions[14] mainly in the relatively small tangential component. No noticeable difference was found in using either of these formulations.

The relative velocity of the flow over the geometric center of a particular cable element is found by averaging the relative velocities of its two end nodes, where the relative velocity of the air over node i is a function of the air velocity as well as the velocity of the node:

$$\|\boldsymbol{v}^i\| = \sqrt{\left(U_X^i - \frac{\mathrm{d}r_X^i}{\mathrm{d}t}\right)^2 + \left(U_Y^i - \frac{\mathrm{d}r_Y^i}{\mathrm{d}t}\right)^2 + \left(U_Z^i - \frac{\mathrm{d}r_Z^i}{\mathrm{d}t}\right)^2} \tag{6}$$

where U_X^i, U_Y^i, and U_Z^i are the local air velocity components at node i due to the mean wind and air turbulence. Once the drag for elements i and $i+1$ are calculated, one-half of each value is applied to the ith node that joins the two elements.

Finally, the equation for the net gravitational force acting on a cable element in the inertial frame is

$$W^i = \rho_c \left(\pi d_c^2 / 4\right) l_u^i g \tag{7}$$

where ρ_c is the density of material of the element.

The equations for internal forces and the drag forces are developed in an elemental body-fixed frame, whereas the equations for the gravitational forces are developed in an inertial frame. The motion equations are written in the inertial frame, and, thus, all forces must be transformed into that frame before inclusion in these equations.

B. Spherical Aerostat and Receiver Housing

The aerostat design for LAR has not yet been finalized and may be spherical or streamlined. Models for both of these types of aerostat are, therefore, considered in this work. Based on an earlier statics analysis of the LAR system,[8] it was expected that the spherical aerostat would not perform as well due to its higher drag coefficient. However, the spherical aerostat would be cheaper to purchase and operate and, thus, was considered worth investigating.

The spherical aerostat is modeled as a single mass at the upper node of the leash, subject to buoyancy, aerodynamic drag (generated by winds and gusts), and gravity. The antenna receiver is located at the upper confluence point of the three tethers and is assumed to be enclosed in a spherical housing. Thus, for both the spherical aerostat and the receiver, the aerodynamic drag can be found from

$$D_s = \tfrac{1}{2}\rho C_d \left(\pi d_s^2 / 4\right) \|\boldsymbol{v}_s\|^2 \tag{8}$$

where D_s is the aerodynamic drag force, d_s is the aerostat or receiver diameter, C_d is the normal drag coefficient, and $\boldsymbol{v}_s$ is the local velocity of the geometric center of the aerostat or receiver, relative to the surrounding air. The variation in drag coefficient of a spherical object[15] from 0.4 to 0.15, depending on the Reynolds number of the flow, was included.

The added mass of the aerostat and receiver were included in the model because they are large. These were calculated as one-half of the displaced air mass of the corresponding spheres.[16]

C. Streamlined Aerostat

The streamlined aerostat modeled is a scaled-up (by a factor of 2.33) version of the Aeros FlightCam aerostat, shown in Fig. 4. The aerostat in Fig. 4 is presently being used in a proof-of-concept demonstration for this project. For modeling purposes, the aerostat is considered to be rigid and capable of six-degrees-of-freedom motion. The model uses a component breakdown method, as outlined by Nahon.[17] The aerostat is considered to be composed of the hull and three aft fins. The forces acting on the aerostat are due to aerodynamics, weight, and buoyancy. Both weight and buoyancy act along the vertical, and their values are considered constant. The aerodynamic forces are calculated for each single component and later summed.

For the fins, the location of the center of pressure is approximated at their one-quarter chord line midway from the base to the tip. The local angle of attack α can be calculated using the relationship

$$\alpha = \tan^{-1}(w/u) \tag{9}$$

where u and w are the local velocities along the chord and normal to it. The fins are approximated as NACA 0018 sections, and the dimensionless lift coefficient is calculated using available empirical data for airfoil shapes. The lift coefficient is then reduced to account for 1) the finite aspect ratio of the fin and 2) the reduction in fin effectiveness due to operation in the disturbed airflow at the rear of the hull. The drag coefficient of the fins is computed as[15]

$$C_D = C_{D0} + C_L^2 / \pi A e \tag{10}$$

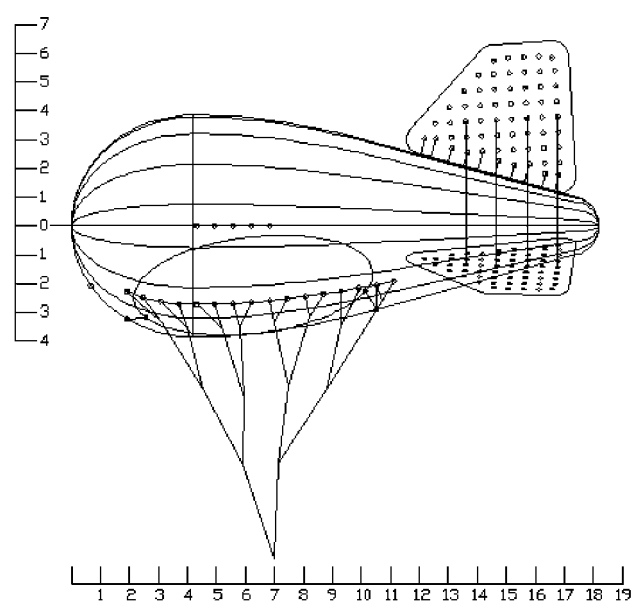

Fig. 4 Aeros FlightCam aerostat.

The lift and drag forces are given by

$$L = \tfrac{1}{2}\rho A_f C_L \|\boldsymbol{V}\|^2, \qquad D = \tfrac{1}{2}\rho A_f C_D \|\boldsymbol{V}\|^2 \tag{11}$$

where $\boldsymbol{V}$ is the local velocity at the center of pressure.

For the hull, the method of Jones and DeLaurier[6] is used to calculate transverse and drag force and a pitch moment about the nose:

$$N_h = q_0[(k_3 - k_1)\eta_k I_1 \sin(2\alpha)\cos(\alpha/2) + (Cd_c)_h J_1 \sin\alpha \sin|\alpha|]$$

$$D_h = q_0\left[(Cd_c)_0 S_h \cos^2\alpha - (k_3 - k_1)\eta_k I_1 \sin(2\alpha)\cos(\alpha/2)\right]$$

$$M_{\text{nose}} = -q_0[(k_3 - k_1)\eta_k I_3 \sin(2\alpha)\cos(\alpha/2) + (Cd_c)_h J_2 \sin\alpha \sin|\alpha|] \tag{12}$$

where $V_B = (u^2 + v^2 + w^2)^{1/2}$, the total velocity of the aerostat, and α is the hull angle of attack. The calculation of these coefficients is based on the hull geometry and is discussed in detail by Lambert.[18] Most of these quantities can be estimated with good confidence using the methods discussed by Jones and DeLaurier.[6] The crossflow drag coefficient was more difficult to estimate accurately, but we found relatively little change in our results with changes in this parameter.

The effective point of application of the hull force is then calculated from the hull moment and lift force. Once all forces are found, they are summed to obtain the total force acting on the aerostat. The moments exerted by these forces are also summed to obtain the total moment acting on the aerostat.

D. Mean Wind and Turbulence

A wind model was incorporated to determine its effect on the tethered aerostat system. It consists of a height-dependent mean wind profile on which are superimposed turbulent gusts that also vary with height. The mean wind U at height h was represented by a power law profile[19] representing the Earth's boundary layer,

$$U = U_g(h/h_g)^{\gamma} \tag{13}$$

where the power law exponent $\gamma = 0.19$ was used to represent conditions in rural areas. A gradient height $h_g = 500$ m was used, at which the mean wind reaches its full speed of U_g.

Turbulent gusts were superimposed on this mean wind. These were generated with the desired gust statistical properties,[19] including turbulence intensity, scale length, and spectra. The turbulence intensities σ_u, σ_v, and σ_w in the three orthogonal directions were

$$\frac{\sigma_u}{U} = \begin{cases} 0.1 & h \geq 300 \text{ m} \\ 0.1 + 4.328 \times 10^{-9}(300 - h)^3 & h < 300 \text{ m} \end{cases}$$

$$\frac{\sigma_v}{\sigma_u} = \begin{cases} 1 & h \geq 300 \text{ m} \\ 0.7 + h/1000 & h < 300 \text{ m} \end{cases}$$

$$\frac{\sigma_w}{\sigma_u} = \begin{cases} 1 & h \geq 300 \text{ m} \\ 0.25 + h/400 & h < 300 \text{ m} \end{cases} \tag{14}$$

whereas the three corresponding scale lengths L_u, L_v, and L_w were

$$L_u = 280(h/h_g)^{0.35}, \qquad L_v = 140(h/h_g)^{0.48}$$

$$L_w = \begin{cases} 0.35h & h \leq 400 \text{ m} \\ 140 & h > 400 \text{ m} \end{cases} \tag{15}$$

and, finally, the three corresponding spectra Φ_u, Φ_v, and Φ_w were taken from a von Kármán model (see Ref. 19) with

$$\Phi_u(\Omega) = \left(\frac{\sigma_u}{U}\right)^2 U^2 \frac{L_u}{\pi} \cdot \frac{1}{\left[1 + (aL_u\Omega)^2\right]^{\frac{5}{6}}}$$

$$\Phi_v(\Omega) = \left(\frac{\sigma_v}{U}\right)^2 U^2 \frac{L_v}{2\pi} \cdot \frac{1 + \frac{8}{3}(aL_v\Omega)^2}{\left[1 + (aL_v\Omega)^2\right]^{11/16}}$$

$$\Phi_w(\Omega) = \left(\frac{\sigma_w}{U}\right)^2 U^2 \frac{L_w}{2\pi} \cdot \frac{1 + \frac{8}{3}(aL_w\Omega)^2}{\left[1 + (aL_w\Omega)^2\right]^{11/16}} \tag{16}$$

where Ω is the wave number and $a = 1.339$. The following procedure was adopted to generate each of the three gust components:

1) Discretize the wave number axis of the spectrum Φ_j into $N = 50$ intervals, each of width $\Delta\Omega_i = 1.2\Delta\Omega_{i-1}$, $i = 1, \ldots, N$, with $\Omega_0 = 0.0001$ and $\Delta\Omega_0 = 0.0001$.

2) Randomly choose a wave number Ω_i within each interval.

3) Randomly choose a phase angle φ_i from 0 to 2π for each component.

4) Evaluate $\Phi_j(\Omega_i)/U^2$.

5) Evaluate $A_i/U = (2\Phi_j \Delta\Omega_i/U^2)^{1/2}$.

6) Evaluate the gust speed:

$$v_g = \sum_{i=1}^{N} \frac{A_i}{U} U \cos(\Omega_i(x - tU) + \varphi_i) \tag{17}$$

where x and t are the position along the mean wind direction and time, respectively. The preceding equation implies the use of a frozen-field approximation[19] to relate temporal and spatial gust correlations.

Steps 1–5 are all implemented offline. Step 6 must be implemented during the dynamics simulation and is a function of position and time.

The procedure is an adaptation of a similar procedure commonly used in the synthesis of water wave heights from standard wave spectra.[20] It is expected that this approach will incorporate the dominant features of the turbulence statistics, though it does have two failings: 1) It neglects the spatial correlations in gusts in the directions perpendicular to the mean wind velocity. 2) It can generate excessive wind accelerations due to the random phase relationship between the wind spectral components. However, these shortcomings in the wind model will lead to conservative results when assessing the system performance.

E. Assembly of the Motion Equations

Once all of the internal and external forces just described have been expressed in the common inertial frame, the equations governing the translational motion of each node can be written as

$$\boldsymbol{M}^i \ddot{\boldsymbol{r}}^i = (\boldsymbol{T}^{i+1} + \boldsymbol{P}^{i+1}) - (\boldsymbol{T}^i + \boldsymbol{P}^i) + \tfrac{1}{2}\left(\boldsymbol{D}^i + \boldsymbol{D}^{i+1} + m_c^i \boldsymbol{g} + m_c^{i+1}\boldsymbol{g}\right) \tag{18}$$

where $\boldsymbol{T}^i$ and $\boldsymbol{P}^i$ are the elastic and damping force vectors generated in the ith element, $\boldsymbol{D}^i$ is the aerodynamic drag force vector on the ith element, and $m_c^i \boldsymbol{g}$ is the gravitational force acting on the ith element. The weight, buoyancy, and aerodynamic lift and drag of the aerostat and receiver are simply added to the appropriate cable nodes (at the lower and upper ends of the leash, respectively). All of the node equations are then assembled with the rotational equations of the aerostat and integrated simultaneously for $\boldsymbol{r}^i$, the position of node i in inertial space, and the Euler angles of the aerostat.

F. Numerical Implementation

The second-order differential equations given by Eq. (18) must now be solved by numerical integration. Each of the t tethers is discretized into n_t elements, resulting in $n_t + 1$ nodes for each tether. However, because the uppermost nodes of all of the tethers are connected together at the confluence point, there are a total of $tn_t + 1$ nodes in the tethers. The leash consists of an additional n_l elements. However, its lowermost node is attached to the confluence point, and its uppermost node is lumped with the aerostat, so that the leash adds only $n_l - 1$ nodes to the system. This results in a total of $tn_t + n_l$ nodes in the system.

Each node is modeled by three second-order ordinary differential equations (ODEs) (one for each nodal degree of freedom). However, the lowermost node of each tether has no differential equations associated with it because its motion is prescribed. The receiver does not add any differential equations because its effect is lumped into the confluence point node. Consideration of the aerostat motion adds six second-order ODEs to the system. Thus, a total of $3(tn_t + n_l - t) + 6$ second-order ODEs are needed to describe the complete system. To apply a numerical integration algorithm in standard form, each second-order ODE is rewritten as two first-order ODEs. This then

leads to a total of of $6(tn_t + n_l - t) + 12$ first-order ODEs to represent the complete system.

The approach used to solve the system of differential equations is taken from Ref. 21. The particular integrator chosen is a fourth-order Runge–Kutta technique with fixed step size.[21] This method gives accurate solutions for a broad range of problems, though not necessarily with optimum efficiency. Because the system of differential equations is large (186 first-order ODEs for $t = 3$, $n_t = 10$, and $n_l = 2$), and the cable material is stiff ($E = 3.74 \times 10^{10}$ Pa), a small time step was used to avoid numerical instabilities and to ensure an accurate solution. Accuracy tests were made to ensure that an appropriate time step was used, ultimately leading to a time step of 1 ms.

III. Winch Control

Winches at the base of each tether are used to keep the receiver in the desired position in presence of wind and turbulence. Each winch is controlled by an independent PID controller that responds to errors in the receiver position, which we presume to be measured accurately. A planar representation of the geometry is shown in Fig. 5.

The desired location of the receiver is at $\boldsymbol{p}_d$, whereas its actual location is at $\boldsymbol{p}$. The location of the jth winch, $j = 1, \ldots, 3$, is at $\boldsymbol{p}_{Wj}$. For each winch, we can, therefore, define the error in the receiver position as

$$e_j = \|\boldsymbol{p} - \boldsymbol{p}_{Wj}\| - \|\boldsymbol{p}_d - \boldsymbol{p}_{Wj}\| \tag{19}$$

Our winch controller can now operate according to

$$\Delta L_j = -\left(k_P e_j + k_D \dot{e}_j + k_I \int e_j \, \mathrm{d}t\right), \qquad j = 1, \ldots, 3 \tag{20}$$

where ΔL_j is the change in length of tether j and the three gains k_P, k_D, and k_I are the same for all tethers because no advantage was found for them to be different.

The motivation behind this approach is that, if the distance from winch j to the receiver is correct, then the receiver lies on a sphere of radius $\|\boldsymbol{p}_d - \boldsymbol{p}_{Wj}\|$ centered at the winch. If all three receiver–winch distances are correct, then the receiver lies at the intersection of those spheres that define the correct desired location of the receiver in three-dimensional space.

A. System Configuration

The numerical simulation based on the preceding model is capable of finding the nonlinear response of the system due to wind disturbances and initial conditions. The system can be configured with either of the two aerostat types, with any number of tethers ($t \geq 3$), and in any configuration (receiver position, wind speed U_g, and wind direction θ_w). The receiver's desired position was at a fixed point on a hemisphere of radius $R = 500$ m whose center lay on the Earth's surface. The winches were each located 1200 m from the hemisphere's center and configured symmetrically 120 deg apart. The desired location of the receiver is specified by its zenith θ_{za} and azimuth θ_{az} angles, shown in Fig. 6. From this geometry, we find that the desired position coordinates of the receiver are

$$\boldsymbol{p}_d = [R\cos\theta_{az}\sin\theta_{za} \quad R\sin\theta_{az}\sin\theta_{za} \quad R\cos\theta_{za}]^T \tag{21}$$

The operating range considered is $0 < \theta_{za} < 60$ deg, $0 < \theta_{az} < 360$ deg, $0 < \theta_w < 360$ deg, and $0 < U_g < 10$ m/s. Results are only shown here for the tritethered arrangement.

The tether and leash consisted of Puget Sound Plasma rope of 1.85-cm diam, with a density of 840 kg/m^3, and a normal drag coefficient of 1.2. The 500-kg receiver was contained in a sphere of 6-m diam; the spherical aerostat had diameter of 19.7 m, a mass of 610 kg, and a net buoyancy of 34,895 N; and the scaled-up Aeros streamlined aerostat had a mass of 4539 kg and a net buoyancy of 34,872 N.

The simulation just described was first validated by comparing its steady-state results against an independently generated statics simulation.[8] All results matched within a fraction of a percent, both with and without steady winds (no turbulence).

B. Gain Optimization for Streamlined Aerostat

The streamlined aerostat was considered first. Gains were chosen to optimize the behavior of the system in term of maximum error and power. These two quantities are defined as

$$E_{\max} = \max\|\boldsymbol{p} - \boldsymbol{p}_d\|, \qquad P_{\max} = \max|T_j \cdot \dot{L}_j| \tag{22}$$

where T_j is the tension at the winch of each tether. To limit the winch power requirements, a bound of 50 kW was imposed that had to be satisfied throughout the operating envelope and cases considered. Several simulations showed a qualitative relationship between the error, power and wind speed, wind direction, zenith angle, and azimuth angle. It was found that both the error and the power tended to increase directly with increases in wind speed or zenith angle, as shown in Tables 1 and 2. Thus, the maximum values of these two parameters (10 m/s and 60 deg) were used to find the worst-case configuration.

With a baseline set of gains, the worst-case configuration, that is, the azimuth angle and wind direction, in terms of power was identified. The controller gains were gradually increased to reduce the

Table 1 Maximum error and power for $\theta_{za} = 0$, $\theta_{az} = 0$, $\theta_w = 0$, and gains = 5, 3, and 1

Wind speed, m/s	Error, cm	Power, kW
2	2.2	1.0
4	7.3	3.3
6	14.8	8.1
8	24.8	15.8
10	36.5	27.1

Table 2 Maximum error and power for $\theta_{az} = 0$, $U_g = 10$ m/s, $\theta_w = 0$, and gains = 5, 3, and 1

θ_{za}, deg	Error, cm	Power, kW
0	36.5	27.1
20	33.9	21.7
40	42.5	24.4
60	75.8	32.9

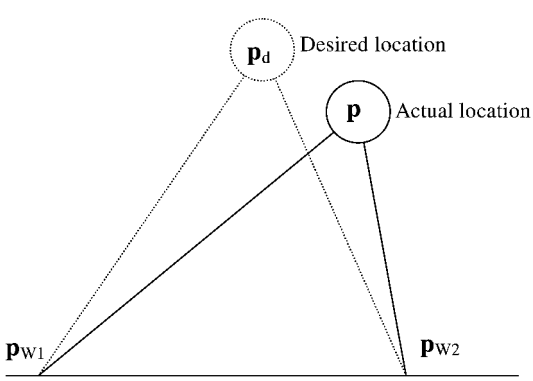

Fig. 5 Control terminology.

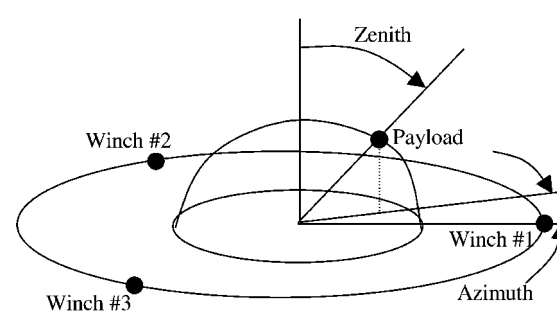

Fig. 6 Geometry of layout.

Table 3 Maximum error (centimeters)/maximum power (kilowatts) for θ_{za} = 60 deg; U_g = 10 m/s; gains = 5, 3, and 1 (lightface type); and gains = 5.3, 3, and 3 (bold type)

	θ_{az}, deg				
θ_w, deg	0	30	60	90	105
0	75.8/32.9	77.3/42.1	78.0/41.6	79.8/43.5	62.8/28.6
30	76.2/33.9	78.6/40.1	70.4/41.3	73.8/40.5	77.4/38.1
60	71.9/33.4	78.0/39.3	81.5/41.7	79.6/42.3	78.1/38.2
90	75.0/34.9	72.5/38.9	79.8/44.1	77.1/43.1	78.1/40.3
120	**80.9/30.4**	80.3/44.2	78.5/44.6	76.9/44.9	77.8/41.1
150	**83.2/31.2**	**80.0/43.3**	85.8/48.0	73.0/45.9	73.4/41.8
180	**83.1/31.8**	**79.0/38.8**	**82.5/47.6**	80.5/48.7	77.6/42.4
210	**82.9/31.2**	**78.4/39.6**	**82.6/41.8**	**78.4/45.8**	62.6/33.6
240	**81.3/30.4**	**78.1/40.0**	**79.1/40.3**	**77.8/42.0**	**83.4/39.3**
270	75.9/35.8	**79.6/46.1**	**82.0/41.4**	**79.1/42.5**	**83.8/39.8**
300	74.8/33.2	80.4/48.1	**82.6/47.7**	**79.8/40.8**	**80.5/36.7**
330	77.4/32.0	73.3/43.6	85.4/48.5	**79.5/42.0**	**78.8/34.7**

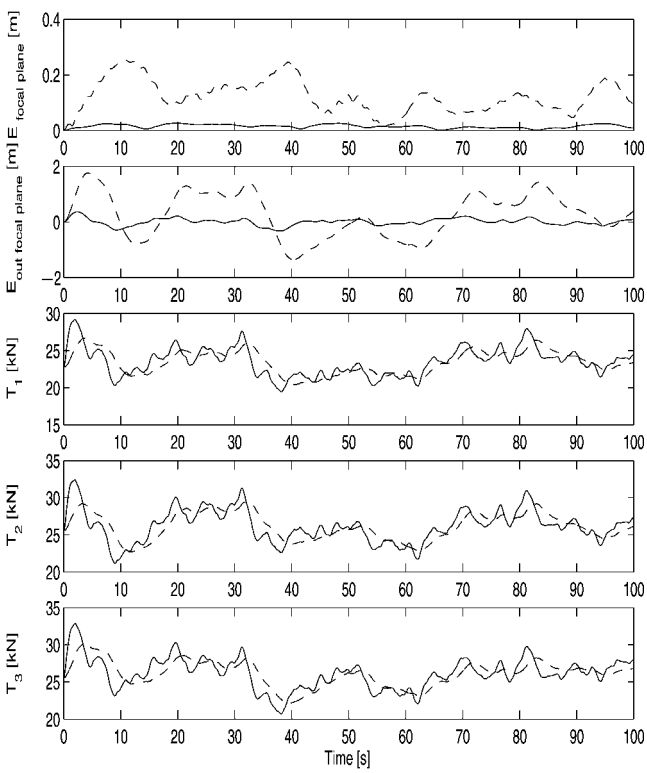

Fig. 7 Comparison of errors and tensions ——, with control and – – –, without control; for these plots, $\theta_{za} = \theta_{az} = 0$, U_g = 10 m/s, $\theta_w = 0$, and gains = 5, 3, and 1.

error, until the power required for the worst-case configuration just exceeded its maximum admissible value. These gains were $k_P = 5$, $k_D = 3$ s, and $k_I = 1$ s^{-1}. With these gains, the power and error were determined for all of the configurations. The results showed that the error was maximum when the wind direction was between $\theta_{az} + 120$ and $\theta_{az} + 240$ deg. It was noted that the configurations with the maximum error did not consume the maximum power. Thus, a second optimization was performed on configurations in the range $\theta_{az} + 120 < \theta_w < \theta_{az} + 240$ deg, to use all of the available power to reduce the maximum error. A second group of gains (5.3, 3, and 3) was determined for that interval. The combined results are shown in Table 3. The results are only shown for azimuth angles up to 105 deg due to symmetry of the system.

Figure 7 shows a comparison of errors and tensions for $\theta_{za} = \theta_{az} = 0$, $U_g = 10$ m/s, $\theta_w = 0$, and gains = 5, 3, and 1, with and without control. The motion is plotted as components in and out of the focal plane (the plane locally tangent to the 500-m hemisphere at the desired aerostat location) because only those errors in the focal plane are of primary importance. When $\theta_{za} = \theta_{az} = 0$, the focal plane is horizontal and the out-of-plane motion is purely vertical. For this configuration, the maximum error is 36.5 cm (Table 1), whereas its maximum component in the focal plane is an order of magnitude less (Fig. 7). The uncontrolled case makes apparent that the system responds little to high-frequency gusts and acts as a natural low-pass filter due to its huge scale.

In summary, we find that the positioning error can be consistently kept below 85 cm throughout the operating envelope. Of course, with more power available at the winches, the control gains could be increased, and the ensuing positioning errors would be further reduced.

C. Spherical Aerostat

Once the streamlined aerostat controller gains had been optimized, the same gains were applied to the system operating with the spherical aerostat. Results for this configuration are shown in Table 4. The maximum error and the power required are much lower than for the streamlined aerostat. The error could be further reduced by increasing the gains until the 50-kW power limit is reached. However, note that this simulation does not include the effects of vortex shedding from the spherical aerostat, a phenomenon that can cause large additional disturbances.[22]

A statics analysis of the LAR system[8] had indicated that the streamlined aerostat should lead to better system performance. Consistent with that investigation, we found that the steady-state forces are generally lower for the streamlined aerostat. However, the variations about the mean, which are a more important issue for dynamic positioning, were higher due to the aerodynamic lift generated by the hull and fins.

Table 5 shows a typical example of the inertial frame components of the leash tension for the streamlined and spherical aerostat. Table 5 shows that the mean forces generated by the streamlined aerostat are generally lower, but that their rms values are higher, especially in the vertical direction. The streamlined aerostat is trimmed to a 4-deg nose-up attitude, which results in a higher mean tension component in the z direction. When trimmed to a level attitude, that mean z tension can be reduced to a level similar to the spherical aerostat, but the rms value is largely unchanged, and the errors remain high.

D. Slewing

A slewing maneuver consists of moving the receiver from one position to another. It is accomplished by changing the lengths of the three tethers on a larger scale than done in the fixed-position control just shown. Slewing can be done with or without the controller active, that is, either open or closed loop.

In the open-loop case, the length of each tether was changed from the value corresponding to the initial position L_0 to the value corresponding to the final position $L_0 + \Delta L$ using a sinusoidal ramp, that is,

$$L = L_0 + \Delta L[t/T - \sin(2\pi t/T)/2\pi], \qquad t \le T$$

$$L = L_0 + \Delta L, \qquad t > T \tag{23}$$

Table 4 Maximum error (centimeters)/maximum power (kilowatts) for θ_{za} = 60 deg; U_g = 10 m/s; gains = 5, 3, and 1 (lightface type); and gains = 5.3, 3, and 3 (bold type)

	θ_{az}, deg				
θ_w, deg	0	30	60	90	105
0	5.8/4.0	6.5/4.6	7.4/6.8	7.1/9.6	5.1/4.6
30	5.1/5.9	6.2/4.5	7.6/4.7	9.1/5.0	6.2/5.7
60	5.1/3.6	5.4/3.6	7.6/4.9	8.7/6.1	6.3/7.1
90	6.0/9.1	5.3/8.4	7.4/4.6	7.2/6.2	7.6/6.4
120	**4.2/3.2**	6.7/9.5	6.6/7.3	9.1/6.5	6.4/6.3
150	**5.7/3.4**	**5.4/8.4**	7.5/11.4	8.1/7.8	6.2/6.2
180	**6.1/4.9**	**5.2/5.7**	**5.5/11.6**	8.9/11.6	7.9/7.4
210	**5.2/3.4**	**5.6/5.9**	**6.7/4.8**	**7.8/9.0**	5.7/5.3
240	**4.1/3.1**	**5.8/4.0**	**7.8/4.6**	**7.3/7.9**	**5.1/6.2**
270	6.5/10.4	**5.2/10.6**	**6.1/8.2**	**7.4/9.6**	**7.4/7.0**
300	5.5/3.8	6.7/12.3	**4.9/11.8**	**7.5/13.1**	**6.2/9.8**
330	5.4/3.4	5.3/4.8	7.2/9.3	**8.6/11.1**	**6.4/5.9**

Table 5 Mean and rms tensions for θ_{za} = 60 deg, θ_{az} = 60, U_g = 10 m/s, θ_w = 300 deg, and gains = 5, 3, and 1

Tension, N	Spherical	Streamlined
Mean/rms in x	−1,236/279	−345/853
Mean/rms in y	2,206/298	841/247
Mean/rms in z	−34,880/162	−38,491/2,393

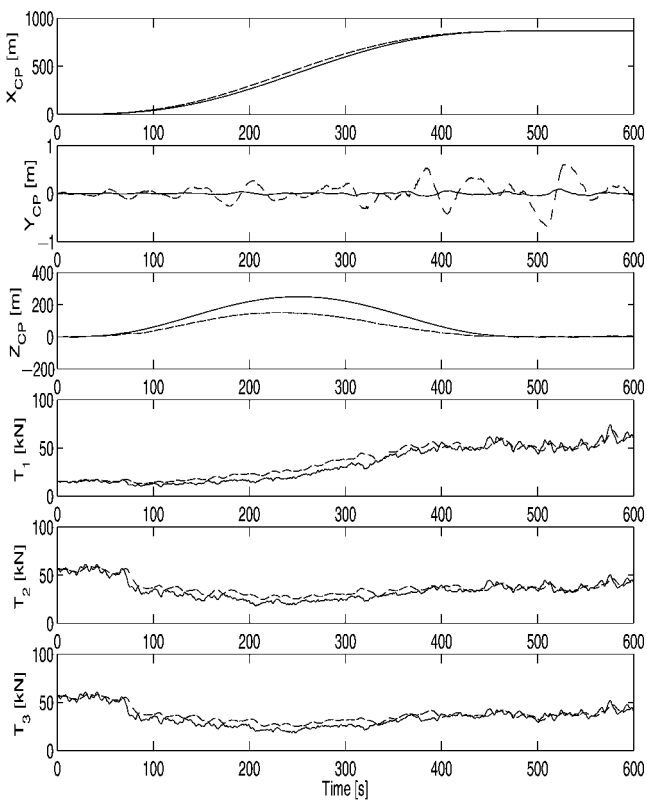

Fig. 8 Comparison of lengths and tensions during slewing ——, with control and – – –, without control; for these plots, θ_{az} = 0, U_g = 10 m/s, θ_w = 0, and gains = 5, 3, and 1.

where T is the desired time to complete the maneuver. The advantage of this function is that the initial and final acceleration are zero; thus, the impact of the maneuver on the system is reduced.

In the closed-loop case, the desired position of the receiver, defined by $\boldsymbol{p}_d$, is changed using a similar function on the zenith and/or azimuth angle. The controller forces the system to follow this variation until the final desired position is reached. Figure 8 shows a comparison of the results for a slewing maneuver, with the streamlined aerostat, from a −60 to +60 deg zenith angle, completed in 500 s. The position of the receiver and the tensions at the winches are shown.

Both methods are effective in guiding the system to its final configuration. In the open-loop case, some oscillations are present at the final configuration due to motion excited during the maneuver. In the closed-loop case, the terminal oscillations are smaller because disturbances during the maneuver are compensated for and, therefore, do not build up. A possible alternative would be to perform the open-loop slewing and then activate the controller when the final position is reached (likely using a ramp on the gains instead of immediately using their final values, to avoid instabilities).

IV. Conclusions

A simulation of a large tethered aerostat system controlled by ground-mounted winches was developed. The computer simulation described here provides an efficient and cost-effective method of determining the effects of different wind conditions and aerostat configurations on the tethered aerostat system described. It was found that the system is relatively insensitive to turbulent gusts and only responds to the lowest-frequency gusts. The simulation was used to optimize the winch control gains and study the relative performance of streamlined and spherical aerostats. It was found that, with 50 kW available at each winch, the receiver could be kept within ∼1 m from its desired location in its worst-case configuration. The positioning error was substantially smaller in other configurations. When the spherical aerostat was used, it incurred smaller errors and used substantially less power. The streamlined aerostat's worse performance was due to the lift generated with gust-induced changes in wind incidence.

References

[1] van de Weygaert, R., and van Albada, T. S., "New Challenges for Cosmology," *The Westerbork Observatory, Continuing Adventure in Radio Astronomy*, edited by E. Raimond and R. Genee, Astrophysics and Space Science Library, Vol. 207, Kluwer Academic, Dordrecht, The Netherlands, 1996, pp. 225–259.

[2] Legg, T. H., "A Proposed New Design for a Large Radio Telescope," *Astronomy and Astrophysics Supplement*, Vol. 130, No. 2, 1998, pp. 369–379.

[3] Carlson, B., Bauwens, L., Belostotski, L., Cannon, E., Chang, Y.-Y., Deng, X., Dewdney, P., Fitzsimmons, J., Halliday, D., Kürschner, K., Lachapelle, G., Lo, D., Mousavi, P., Nahon, M., Shafai, L., Stiemer, S. F., Taylor, R., and Veidt, B., "The Large Adaptive Reflector: A 200-m Diameter, Wideband, cm-Wave Radio Telescope," *Radio Telescopes—Proceedings of SPIE Meeting 4015*, SPIE Press, Bellingham, WA, 2000, pp. 33–44.

[4] Jones, S. P., and Krausman, J. A., "Nonlinear Dynamic Simulation of a Tethered Aerostat," *Journal of Aircraft*, Vol. 19, No. 8, 1982, pp. 679–686.

[5] Jones, S. P., "Nonlinear Dynamic Simulation of a Moored Aerostat," *Proceedings of the 7th AIAA Lighter-than-Air Technology Conference*, AIAA, New York, 1987, pp. 72–77.

[6] Jones, S. P., and DeLaurier, J. D., "Aerodynamic Estimation Techniques for Aerostats and Airships," *Journal of Aircraft*, Vol. 20, No. 2, 1983, pp. 120–126.

[7] Badesha, S., and Jones, S. P., "Aerodynamics of the TCOM 71M Aerostat," *Proceedings of the 10th AIAA Lighter-than-Air Technology Conference*, AIAA, New York, 1993, pp. 36–42.

[8] Fitzsimmons, J. T., Veidt, B., and Dewdney, P. E., "Steady-State Analysis of the Multi-Tethered Aerostat Platform for the Large Adaptive Reflector

Telescope," *Radio Telescopes—Proceedings of SPIE Meeting 4015*, SPIE Press, Bellingham, WA, 2000, pp. 476–488.

[9]Leclaire, R. C., and Rice, C. B., "The Local Motions of a Payload Supported by a Tri-tethered Natural Shape Balloon," U.S. Air Force Cambridge Research Lab., Rept. AFCRL-TR-73-0748, Bedford, MA, 1973.

[10]Leclaire, R. C., and Schumacher, H. L., "Local Motions of a Payload Supported by a Nolaro Tri-Tethered Balloon," *Proceedings of the Eighth AFCRL Scientific Balloon Symposium*, Air Force Cambridge Research Lab., Bedford, MA, 1974, pp. 233–255.

[11]Driscoll, F., Lueck, R., and Nahon, M., "Development and Validation of a Lumped-Mass Dynamics Model of a Deep-Sea ROV System," *Applied Ocean Research*, Vol. 22, No. 3, 2000, pp. 169–182.

[12]Buckham, B., and Nahon, M., "Formulation and Validation of a Lumped Mass Model for Low-Tension ROV Tethers," *International Journal of Offshore and Polar Engineering*, Vol. 11, No. 4, 2001, pp. 282–289.

[13]Hamilton, J. M., "Vibration-Based Techniques for Measuring the Elastic Properties of Ropes and the Added Mass of Submerged Objects," *Journal of Atmospheric and Oceanic Technology*, Vol. 17, No. 5, 2000, pp. 688–697.

[14]Hoerner, S. F., *Fluid-Dynamic Drag*, Self-published, Midland Park, NJ, 1958, pp. 3–11.

[15]McCormick, B. W., *Aerodynamics, Aeronautics and Flight Mechanics*, Wiley, New York, 1995, pp. 158–175.

[16]Newman, J. N., *Marine Hydrodynamics*, MIT Press, Cambridge, MA, 1989, p. 144.

[17]Nahon, M., "A Simplified Dynamics Model for Autonomous Underwater Vehicles," *Proceedings of the 1996 IEEE Symposium on Autonomous Underwater Vehicle Technology*, IEEE Publ., Piscataway, NJ, 1996, pp. 373–379.

[18]Lambert, C., "Dynamics Modeling and Conceptual Design of a Multi-Tethered Aerostat System," M.Sc. Thesis, Dept. of Mechanical Engineering, Univ. of Victoria, Victoria, BC, Canada, Jan. 2002.

[19]Etkin, B., *Dynamics of Atmospheric Flight*, Wiley, New York, 1972, pp. 529–543.

[20]Fossen, T. I., *Guidance and Control of Ocean Vehicles*, Wiley, New York, 1994, pp. 60–62.

[21]Press, W. H., Teukolsky, S. A., Vetterling, W. T., and Flannery, B. P., *Numerical Recipes in C*, Cambridge Univ. Press, Cambridge, England, U.K., 1992, pp. 710–714.

[22]Govardhan, R., and Williamson, C. H. K., "Vortex-Induced Motions of a Tethered Sphere," *Journal of Wind Engineering and Industrial Aerodynamics*, Vols. 69–71, 1997, pp. 375–385.